JOURNAL OF SANDWICH STRUCTURES & MATERIALS

*Standard Article*

*Journal of Sandwich Structures and Materials*
0(00) 1–26

DOI: 10.1177/1099636215603692
jsm.sagepub.com
SAGE

# Single- and double-layer aluminum corrugated core sandwiches under quasi-static and dynamic loadings

**Cenk Kılıçaslan, İsmet K Odacı and Mustafa Güden**

**Abstract**

The crushing of single- and double-layer zig-zag trapezoidal corrugated core sandwiches was investigated experimentally and numerically at quasi-static and dynamic rates. The buckling stress of sandwiches increased when the rate increased from quasi-static to dynamic. The increased buckling stresses were ascribed to the micro-inertial effects, which altered the buckling mode of the core from three plastic hinges to higher number of plastic hinge formations. The initial buckling stress was numerically shown to be imperfection sensitive when the imperfection size was comparable with the buckling length. The numerical buckling stresses of zig-zag and straight corrugated cores were similar, while higher inertial effects were found in triangular corrugated core.

**Keywords**

Corrugated, sandwich panel, aluminum, simulation, crushing, numerical, impact

## Introduction

The periodic cellular metal constructions encompass the group of materials with the various topologies including corrugations and lattice trusses. These light weight periodic constructions have wide range of engineering applications and are often required for the multi-functionality [1]. Either in the form of single- or multi-layer form, the use of cellular metal constructions is certainly advantageous, partly due

Dynamic Testing and Modeling Laboratory, Department of Mechanical Engineering, Izmir Institute of Technology, Gülbahçe Köyü, Urla, Izmir, Turkey

**Corresponding author:**
Mustafa Güden, Department of Mechanical Engineering, İzmir Institute of Technology, İzmir, Turkey.
Email: mustafaguden@iyte.edu.tr

to their simple manufacturing routes and partly due to their comparable mechanical properties with those of commonly used lightweight cores such as metal foams [2]. The recent experimental and numerical investigations on the periodic cellular metal constructions have concentrated on the impact and blast loading. The investigated constructions included pyramidal truss [2–5], Y-frame [6–8], V-frame [2,6,8,9] and diamond lattice [10]. These studies have provided important information on the mechanical properties and operative deformation modes of the periodic cellular metal constructions at various impact velocity regimes. The dynamic buckling of the columnar structures may be considered in three different velocity regimes as outlined by McShane et al. [11]: (i) low velocities: the plastic buckling is delayed by lateral inertia, (ii) intermediate velocities: the buckling occurs behind an axial shock wave propagating along the column and, (iii) high velocities: the impact velocity exceeds the plastic wave. The increased crushing strengths of the cellular structures at increasingly high deformation rates are ascribed to the micro-inertial effects. Calladine and English [12] classified the energy absorbing structures as Type I and Type II. Type I structures show a flat-topped load–displacement curve, while Type II structures show an initial peak following a softening behavior. Type II structures were found to be more sensitive to impact velocity than Type I structures [12]. The increased deformation forces at increasing deformation rates in the compression of aluminum honeycomb structures through out of plane [13], metallic columnar structures [14], aluminum foams [13,15] and balsa wood in the axial direction [16,17] were reported to result from the micro-inertial effects. V-frame corrugated structures were shown to be more inertia sensitive than Y-frame, as the deformation in V-frame structure is the stretching governed buckling, while in Y-frame core it proceeds with the bending of one of the legs [4]. It was also shown that U-, X- and V-frame cores exhibiting buckling mode of deformation showed higher crushing strengths and energy absorptions than Y-frame cores exhibiting the bending mode of deformation [18]. The sandwich panels constructed using the periodic cellular metal constructions are attractive both for the impact load mitigation such as blast loading, where the large amount of blast energy is required to be absorbed by the progressive crushing of the core, and for the heat exchange media, where the heat dissipation is request in a relatively small space [1].

The aim of the present study was to investigate both experimentally and numerically the quasi-static and dynamic axial crushing response of layered single- and double-layer 1050 H14 aluminum zig-zag trapezoidal corrugated core sandwich panels. One potential application of zig-zag corrugated cores is an energy absorber in the constructions of the ammunition store walls. The constructed corrugated sandwiches absorb the blast through the deformation of the corrugated layers, provide impact protection against debris by the interlayer sheets and supply coolant to extinguish any fire due to zig-zag formation (partial coolant circulation) [19]. Previous studies on the same core topology showed that these structures had also potentials of distributing the incoming impulse laterally to a larger deformation area [20]. More, corrugated core layers can be easily manufactured through versatile and conventional sheet metal forming processes as compared to conventional

porous and lattice core structures. The performance of these structures especially against the blast and impact loadings can be improved by increasing the level of understanding of deformation mechanism of single- and double-layer structures at quasi-static and dynamic loading rates. The effects of fin imperfections on the deformation behavior were also investigated both experimentally and numerically. And lastly, the crushing responses of zig-zag trapezoidal, straight trapezoidal and triangular corrugated core sandwiches were compared.

## Sandwich structure construction and experiments

The tested single- and double-layer corrugated core sandwich structures consisted of 1050 H14 aluminum trapezoidal zig-zag corrugated fin layers (Figure 1(a)), aluminum interlayer sheets and aluminum face sheets. The drawing of a part of the fin layer is shown in Figure 1(b). The height, width and thickness of the fin layer used in the sandwich constructions are sequentially 9, 5 and 0.135 mm. The thicknesses of 1050 H14 aluminum interlayer sheets and face sheets were 0.5 mm and 1.5 mm, respectively. The density of corrugated fin layer excluding the interlayer and face sheets was 115 kg $m^{-3}$, corresponding to a relative density of 0.042. The corrugated core sandwiches were prepared in single-layer (Figure 2(a)): one fin layer with two face sheets and double-layer configurations (Figure 2(b)): two fin layers with one interlayer sheet and two face sheets. The sandwiches were assembled using a polyurethane adhesive (Henkel Thomsit R710) under a weight of 5 kg. The quasi-static compression tests on the sandwiches were conducted at the strain rates of $10^{-3}$, $10^{-2}$ and $10^{-1}$ $s^{-1}$. The square cross-sectioned single- and double-layer compression test specimens were 25 mm in width and 12 and 22 mm in height, respectively. The quasi-static tension test on 1050 H14 aluminum sheets and compression tests on corrugated sandwiches were performed in a Shimadzu universal testing machine.

The quasi-static tensile stress–strain behavior of 1050 H14 aluminum sheets were determined at strain rate of $10^{-3}$ $s^{-1}$. The tension test specimens were prepared in accord with ASTM E8M-04 Standard [21]: the gage length and thickness were 60 and 1.5 mm, respectively. A video extensometer synchronized with the mechanical testing machine was used to measure the axial displacement.

The dynamic tests were performed on the single- and double-layer sandwiches using a strain-gaged direct impact Split Hopkinson Pressure Bar (SHPB) set-up [4]. In these so-called modified SHPB tests, one of the faces of the sandwich specimen was attached to the end of the incident bar and the striker bar was fired through the specimen with an initial velocity. The SHPB set-up was made of 7075 T6 Al alloy bars (40 mm in diameter), with the striker bar length of 300 mm and incident bar length of 1000 mm (Figure 3). The elastic modulus and density of bar material are 71.7 GPa and 2810 kg $m^{-3}$, respectively. Figure 3 shows the picture of the direct SHPB test set-up. The stress wave on the incident bar is measured by means of 350 Ω foil strain gages mounted on the incident bar in a full Wheatstone-bridge configuration. The bridge input voltage is provided with

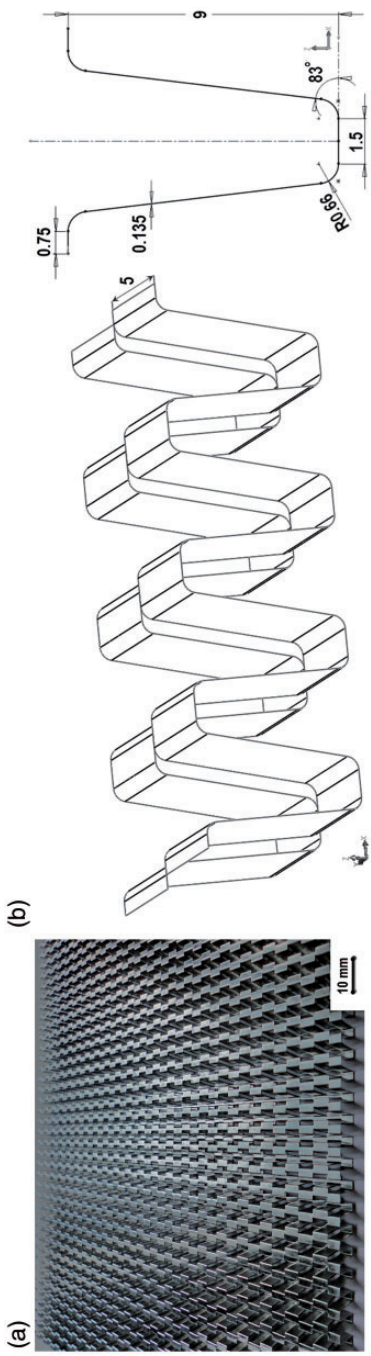


**Figure 1.** (a) a corrugated fin layer and (b) geometric variables of corrugated fins.

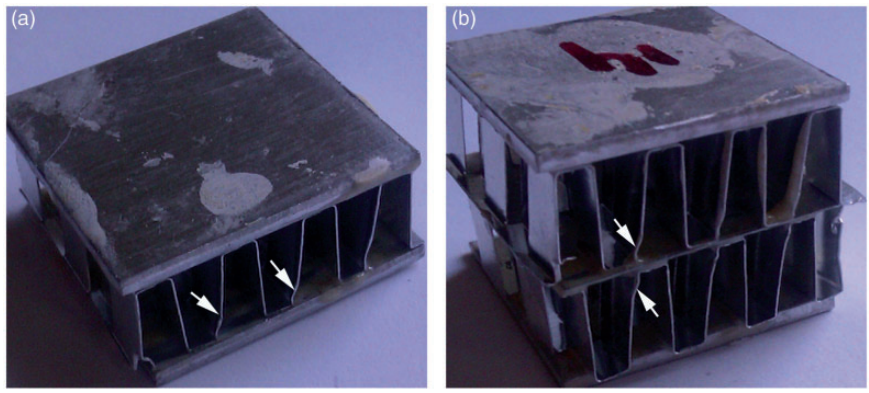


**Figure 2.** (a) single- and (b) double-layer sandwich samples.

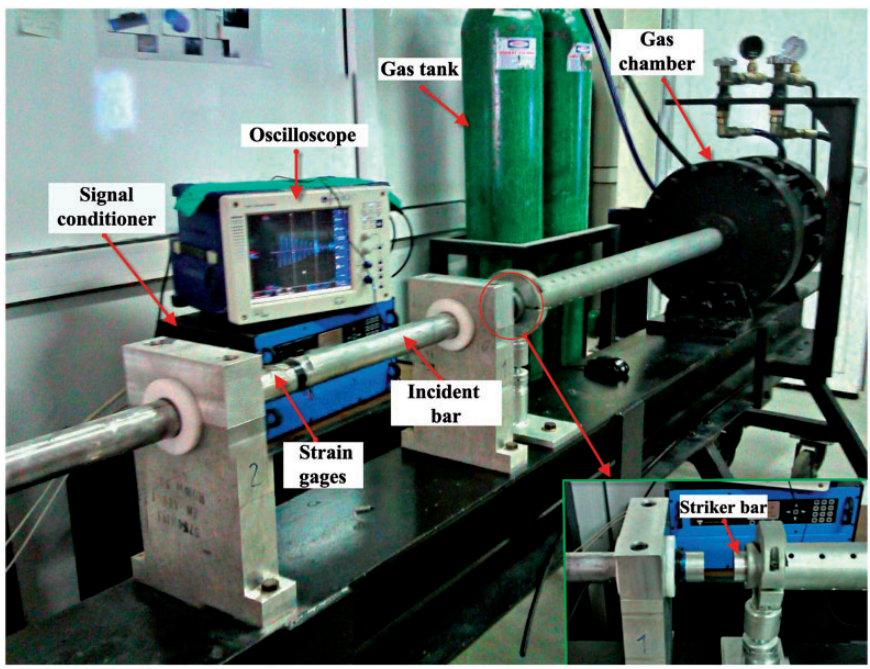


**Figure 3.** Direct SHPB test set-up.

an amplifier/conditioner and an oscilloscope is used to record the output bridge voltage. In a typical test, the gas chamber is filled with nitrogen gas and the release of the gas chamber fires the striker bar onto the incident bar end. The distance between the end of the incident bar and the location of the full-bridge was 500 mm. The loading of the specimen during the test was captured using a high-speed

camera (Fastcam Photron) at 20,000 fps. The velocity of the striker bar was adjusted by the chamber gas pressure and measured using laser-velocity gates located at the exit of the gun chamber barrel. The tests were performed at the striker velocity ($v_0$) of $\sim 18\,\mathrm{m\,s^{-1}}$. The nominal stress ($\sigma$) in the impacted sample (transmitted to the incident bar) was calculated as

$$\sigma(t) = \frac{E_b A_b}{A_s} \varepsilon_t(t) \tag{1}$$

and the nominal strain ($\varepsilon$) and in the sample was calculated as

$$\varepsilon = \frac{v_0 t}{H} \tag{2}$$

where $E_b$, $A_b$ and $A_s$ are the elastic modulus of the bar and sample and bar cross-sectional areas, respectively. $\varepsilon_t$ is the strain measured on the incident bar, $t$ is the time and $H$ is the initial height of the specimen.

## Numerical modeling

The simulations of the quasi-static and dynamic tests were performed in the non-linear explicit finite element code of the LS-DYNA [22]. The 3D geometrical models were implemented in the simulations. As shown by arrows in Figure 2(a) and (b), imperfections on the fin wall were formed during handling and assembling of the fin layers for sandwich construction. Two dominant imperfections as fin wall bending and fin wall bulging were noted and implemented into the numerical models. In order to create imperfect core models, high-resolution photographs of core walls were taken vertically and then imported to a CAD software. Fin wall bending imperfection was introduced to the half of the core with a deviation angle of 6.5° from the original position of the fin wall as shown in Figure 4(a). The numerical models were implemented using the bending-type imperfection, while a part of imperfect models were also modeled with bulge-type imperfection having a deviation angle of 2° to determine the effect of the imperfection length on the crushing stresses (Figure 4(b)). The perfect models of single-layer sandwiches with and without adhesive (polyurethane) layer and the double-layer sandwich without adhesive layer are sequentially shown in Figure 5(a) to (c). The corresponding imperfect models of the single- and double-layer sandwiches are sequentially shown in Figure 5(d) to (f). The effect of the adhesive layer on the stress–strain behavior of the sandwiches was assessed with the implementation of the single-layer models with adhesive layers between the face sheets and corrugated fin layer (Figure 5(b) and (e)).

The trapezoidal corrugated fin layers (Figure 6(a)) were meshed using Belytschko-Tsay shell elements with five integration points. The interlayer and face sheets were modeled using the constant stress solid elements. The increased

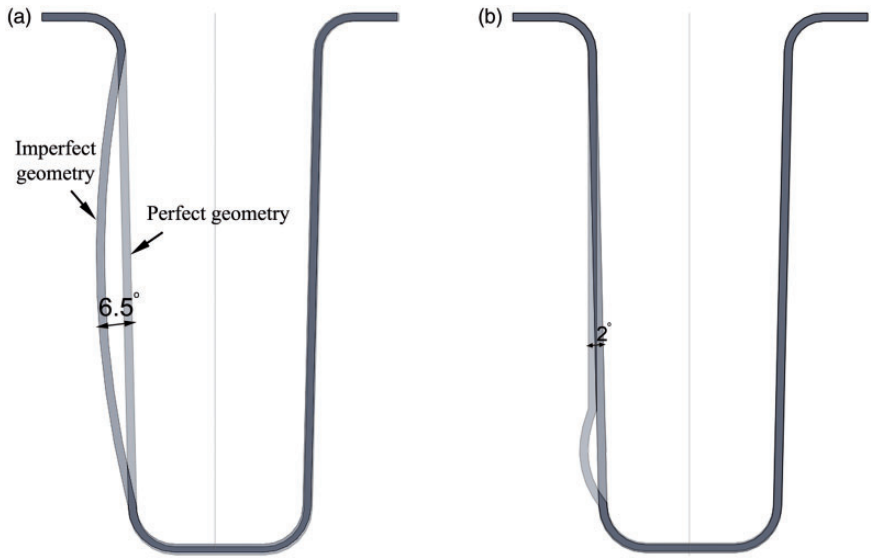


**Figure 4.** Numerical fin wall imperfections (a) fin wall bending and (b) fin wall bulging.

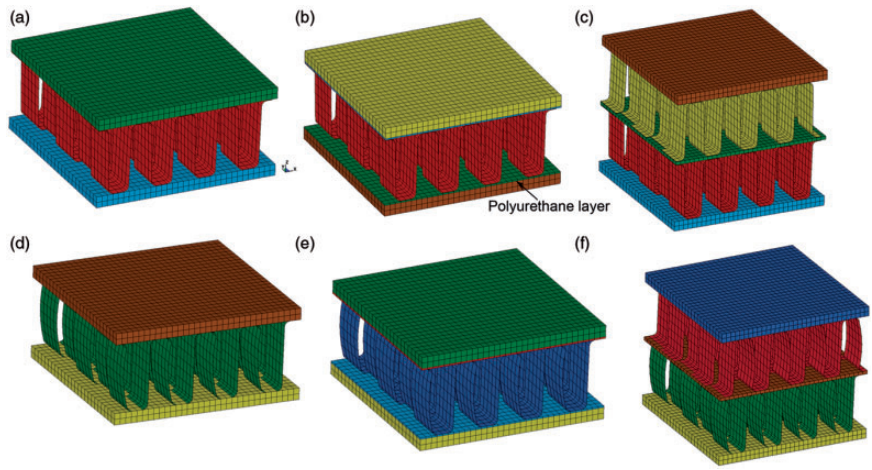


**Figure 5.** Perfect numerical models of (a) single-layer, (b) single-layer with polyurethane layers and (c) double-layer sandwiches and imperfect numerical model of (d) single-layer, (e) single-layer with polyurethane layers and (f) double-layer sandwiches.

number of integration points in the shell elements generally leads to prolonged CPU times. On the other side, the number of integration points should be higher than two, in order to increase the accuracy of the models in the case of dominant buckling deformation mode [23]. In addition, the finite element meshes of the

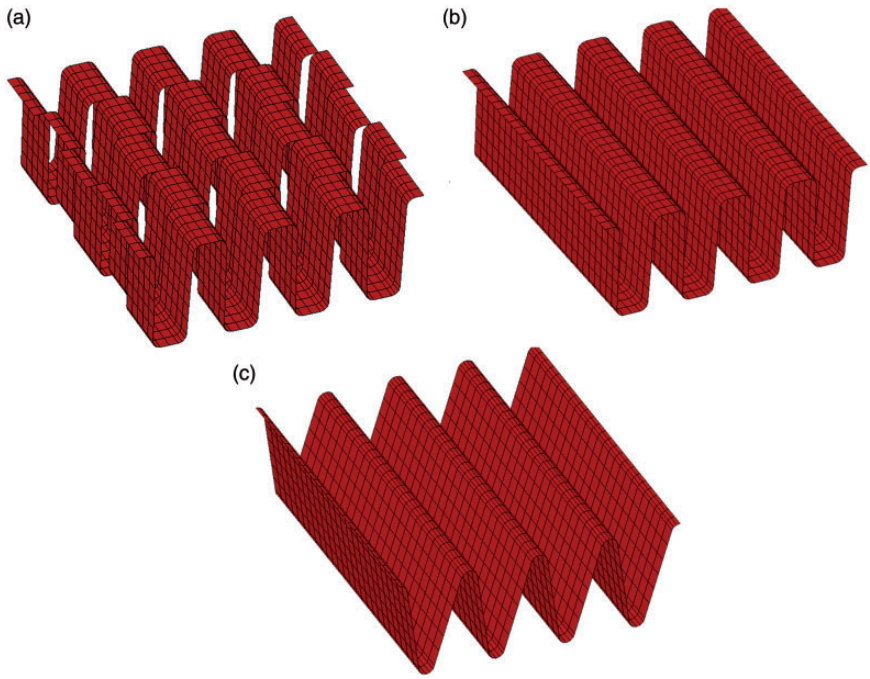


**Figure 6.** Perfect models of corrugated fin layers: (a) zig-zag, (b) straight and (c) triangular.

corrugated fin layers and interlayer-face sheets have to coincide with each other in order to define tied contacts. This naturally limits the use of arbitrary-defined mesh distribution and element sizes. The effect of element size on the numerical results was assessed by implementing (i) mesh model-1 comprising 960 shell and 660 solid elements, (ii) mesh model-2 comprising 2800 shell and 3300 solid elements and (iii) mesh model-3 comprising 10,800 shell and 9900 solid elements in the SHPB models of single-layer sandwich specimen. The quasi-static and dynamic loading rate compression of the straight trapezoidal (Figure 6(b)) and triangular perfect corrugated (Figure 6(c)) single-layer sandwich structures were also modeled in order to determine the effect of fin geometry on the crushing strength.

MAT_SIMPLIFIED_JOHNSON_COOK material model, material type 98, was used to model 1050 H14 aluminum alloy. Johnson and Cook (JC) flow stress model is given as [24]

$$\sigma = [A + B\varepsilon^n]\left[1 + c\ln\left(\frac{\dot{\varepsilon}}{\dot{\varepsilon}_0}\right)\right]\left[1 - (T^*)^m\right] \tag{3}$$

where $\sigma$, $\varepsilon$, $\dot{\varepsilon}$ and $\dot{\varepsilon}_0$ are the effective stress, effective plastic strain, strain rate and reference strain rate, respectively. $A$, $B$, $n$, $c$ and $m$ are the model parameters. The last term $T^*$ is expressed as

$$T^* = \frac{T - T_r}{T_m - T_r} \tag{4}$$

where $T$ is the temperature and $T_r$ and $T_m$ are the reference and melting temperatures, respectively. Material type 98 does not take into account temperature effect expressed in the last bracket of equation (3). As aluminum alloys are known to have low-strain rate sensitivity up to strain rates of $1000\,s^{-1}$ at room temperature [25], the second bracket of equation (3) is also omitted in the material model. The polyurethane adhesive layer was modeled using the MAT01_ELASTIC material model ($E = 69$ MPa and $\upsilon = 0.25$). The thickness of the adhesive layer was taken as 0.2 mm. The contacts between core, adhesive layer, interlayer sheets and face sheets were assumed to be perfectly bonded and defined by TIED_NODES_TO_SURFACE contact algorithm. The self-contacting interfaces were defined by ERODING_SINGLE_SURFACE contact.

Figure 7(a) shows the finite element model of the quasi-static compression test set-up. The model consists of the top and bottom compression test platens and the specimen. Each compression test platen was modeled using 19,200 constant stress solid elements with MAT20_RIGID material model ($E = 210$ GPa and $\upsilon = 0.3$). In the model, the rotations and the movement of the compression platens were fully constrained, except the axial motion of the top platen in the z-direction. The axial velocity of the top platen was kept constant, the same as the experiments and defined by PRESCRIBED_MOTION_RIGID card. The contact between compression test platens and the specimen was defined by AUTOMATIC_SURFACE_TO_SURFACE contact. Since the total CPU time for the quasi-static test solutions was relatively long [26], the mass scaling was applied in the quasi-static simulations by defining 1000 times higher positive time steps in contrast to the initial time step given by LS-DYNA, which decreased total CPU time approximately 700 times. The finite element model of the direct SHPB impact testing is shown in Figure 7(b). The contact area between the striker bar and the specimen was meshed with 2 mm size elements, while the rest of the bars were meshed with 7 and 17 mm size elements. The incident bar was modeled with 20 mm size elements. The models of striker and incident bar consisted of 23,660 and 33,800 constant stress solid elements, respectively. The striker and incident bars were modeled using MAT01_ELASTIC material model. The axial movement and the rotations of the striker and incident bars were constrained in all directions, except the axial movement of the striker bar in the z-direction. The striker bar velocity was defined in the model using VELOCITY_GENERATION in LS-DYNA. The contact between bars and the specimen was defined by AUTOMATIC_SURFACE_TO_SURFACE contact. The contact between bars was defined by AUTOMATIC_SINGLE_SURFACE. The friction coefficient was set to 0.3 in all contact definitions. The stress values on the incident bar were calculated on the bars from an element located at the same distance with the strain gages in the experiments.

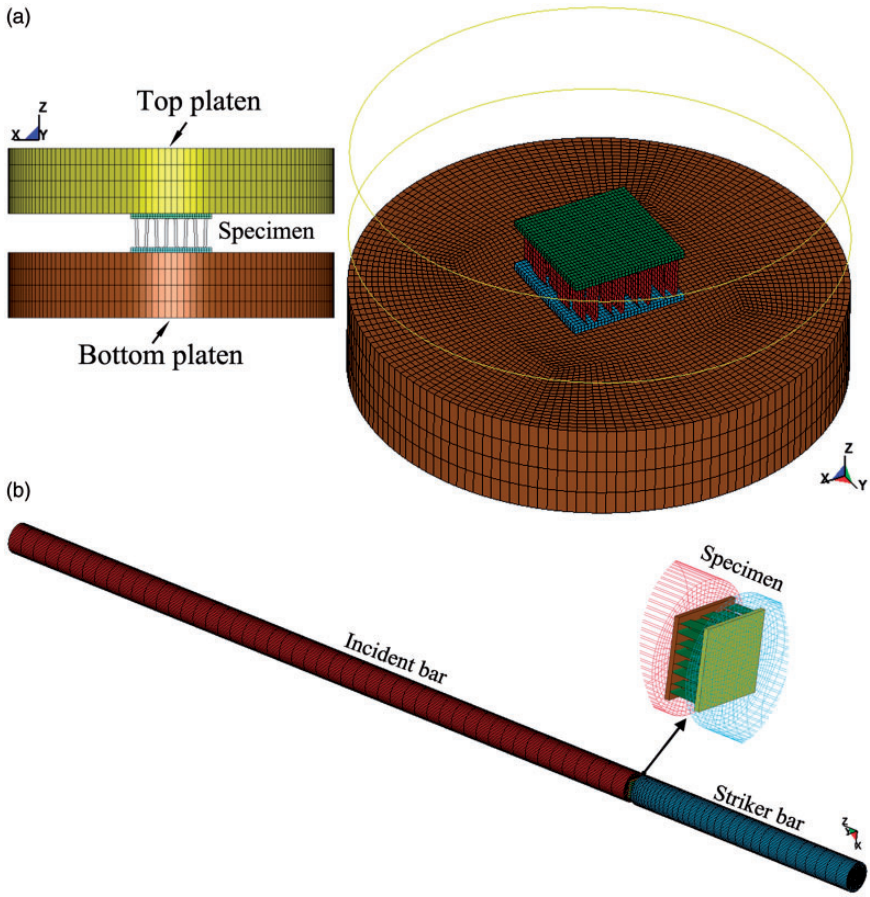


**Figure 7.** Finite element models of (a) quasi-static compression and (b) direct SHPB test set-up.

## Results and discussions

### *Determination of JC coefficients of 1050 H14 Al alloy*

The experimental and JC model true stress-true plastic strain curves of 1050 H14 aluminum alloy are shown in Figure 8. The JC model parameters of the alloy were determined by fitting the first bracket of equation (3) to the experimental true stress-true plastic strain curves. The experimental curves were obtained by averaging at least three tests. The JC flow stress model parameters of 1050 H14 alloy are determined as $A = 102\,\text{MPa}$, $B = 97.2\,\text{MPa}$, $n = 0.18$ and $\varepsilon_f = 0.62$.

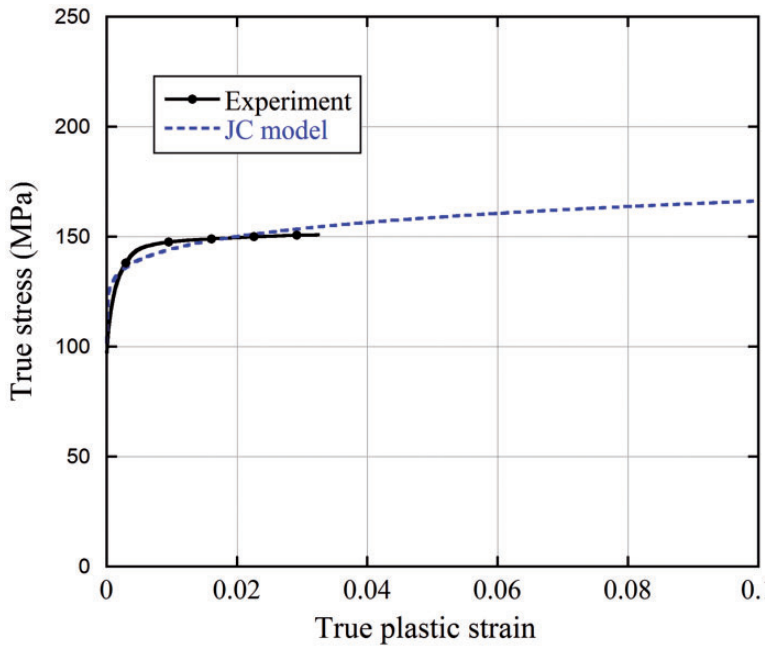


**Figure 8.** Experimental and JC model true stress versus true plastic strain curves of 1050 H14 Al alloy.

## *Effects of element sizes and core imperfection on numerical results*

Experimental nominal stress–strain curve of single-layer sandwich tested in SHPB is shown in Figure 9(a) with the results of numerical models having different element sizes. The initial and second experimental peak stresses were found to be 1.36 and 1.8 MPa, respectively. As seen from the figure, the initial peak stress was well predicted by mesh model-1 and mesh model-2 as 1.3 and 1.25 MPa. However, mesh model-3 failed to predict the initial peak stress accurately, 0.84 MPa. The second peak stress was predicted as 1.37 MPa by mesh model-1 and 2, while mesh model-3 gave a result of 0.87 MPa which is lower than the experimental value. Due to the large number of fluctuations on the stress values, it is hard to compare the curves properly. For clarification, energy versus nominal strain curves of the experiment and simulations were given in Figure 9(b). As depicted in the figure, the experimental energy curve was very well approximated by the mesh model-2 and the mesh model-3. When the results of initial and second peak stress were considered, it is convenient to use mesh model-2. Mesh model-2 also requires~79% lower CPU time in contrast to mesh model-3. Therefore, further simulations were implemented using the mesh model-2. Following modeling efforts focused on the simulation of single-layer sandwich structure using perfect and imperfect core models with and

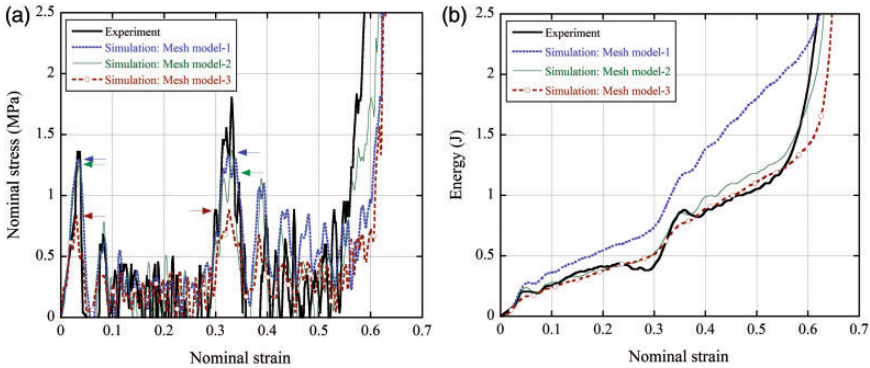


**Figure 9.** (a) Experimental and numerical (a) nominal stress–strain and (b) energy-nominal strain curves of single-layer sandwich at $18\,m\,s^{-1}$ predicted by the models with three different mesh sizes.

without polyurethane adhesive layers at quasi-static ($1.2 \times 10^{-3}$ $m\,s^{-1}$) loading rate. Figure 10(a) shows the early deformation region of the experimental and simulation nominal stress–strain curves of the single-layer sandwich structure. As shown in Figure 10(a), the initial peak stresses of three tests vary between 0.73 and 0.91 MPa. However, the simulation with the perfect model resulted in a higher peak stress (1.25 MPa) and a higher elastic modulus than that of the experiment. The perfect and imperfect models with polyurethane layer resulted in relatively lower elastic moduli. The imperfect model, on the other side, gave a peak stress of 0.84 MPa and an elastic modulus, comparable with those of the experiments. The post-buckling stresses of the perfect model without and with polyurethane layer were also higher than those of the experiments, while the post-buckling stresses of the imperfect models were comparable with those of the experiments (Figure 10(b)). Since the imperfect model with polyurethane layer yielded relatively lower elastic modulus, the following numerical simulations were carried out with the imperfect model. Above results indicated that the compression stresses of the single-layer sandwich structure are imperfection sensitive (bending-type imperfection) at quasi-static loading rates, as similar with the diamond lattice cores reported previously by Cote et al. [10]. Figure 10(c) shows the variations of the striker and the face sheet velocity with time both experimentally and numerically. Experimental velocity variations of the striker and the face sheet were determined from the processing of the photographs taken by high-speed camera. The striker velocity remained constant at $18\,m\,s^{-1}$ during the deformation. Experimental velocity of the face sheet almost stayed constant at $18\,m\,s^{-1}$ until time of 250 μs, and then gradually decreased to $\sim 17\,m\,s^{-1}$ at the end of the deformation. In the numerical simulation, face sheet experienced an initial peak in velocity though the impact of the striker then decreased to the velocity of striker.

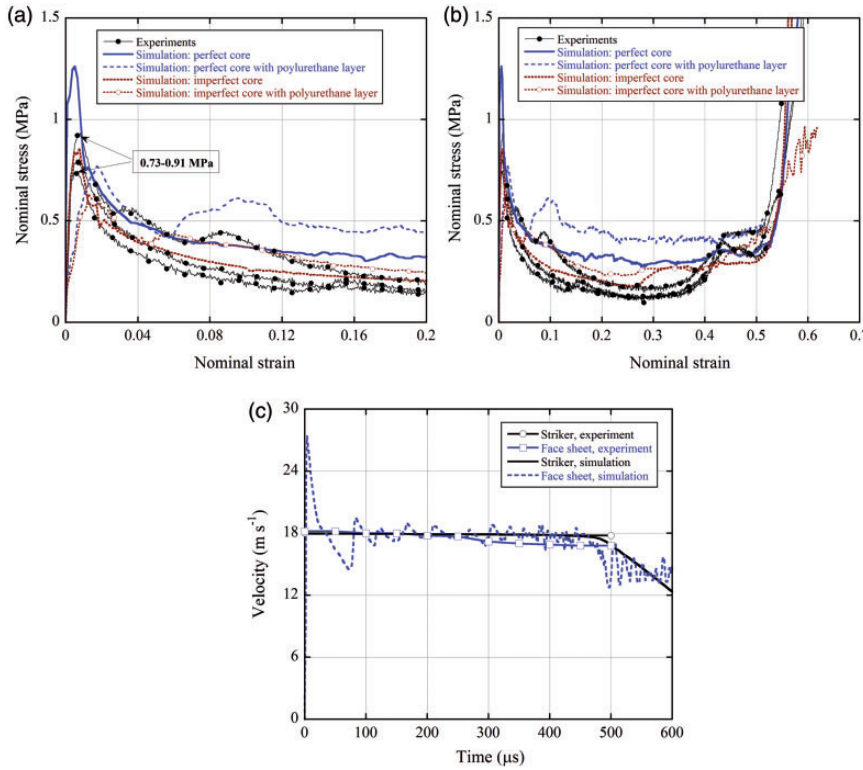


**Figure 10.** (a) and (b) Experimental, perfect and imperfect numerical nominal stress–strain curves of single-layer sandwich at $1.2 \times 10^{-3}$ m s$^{-1}$, and (c) experimental and numerical variation of the striker and face sheet velocity with time in SHPB test.

## *Crushing of single- and double-layer corrugated sandwiches at quasi-static and dynamic loading rates*

The quasi-static ($1.2 \times 10^{-5}$, $1.2 \times 10^{-4}$ and $1.2 \times 10^{-3}$ m s$^{-1}$) and dynamic (18 m s$^{-1}$) experimental and numerical nominal stress–strain curves of the single-layer sandwiches are shown in Figure 11 for comparison. The quasi-static and dynamic compression of the single-layer specimen is much similar to that of a typical strut like structure: following an initial peak stress resulting from the buckling instability of the fin walls, the stress values decrease steeply. The increasing loading rate from $1.2 \times 10^{-5}$ m s$^{-1}$ to 18 m s$^{-1}$ increased the buckling stress from 0.95 MPa to 1.35 MPa, showing a velocity dependent initial crushing stress behavior of the single-layer sandwich. Figure 12(a) and (b) and Figure 13(a) and (b) show the experimental and numerical deformed pictures of the quasi-statically ($1.2 \times 10^{-3}$ m s$^{-1}$) and dynamically (18 m s$^{-1}$) tested single-layer specimens and

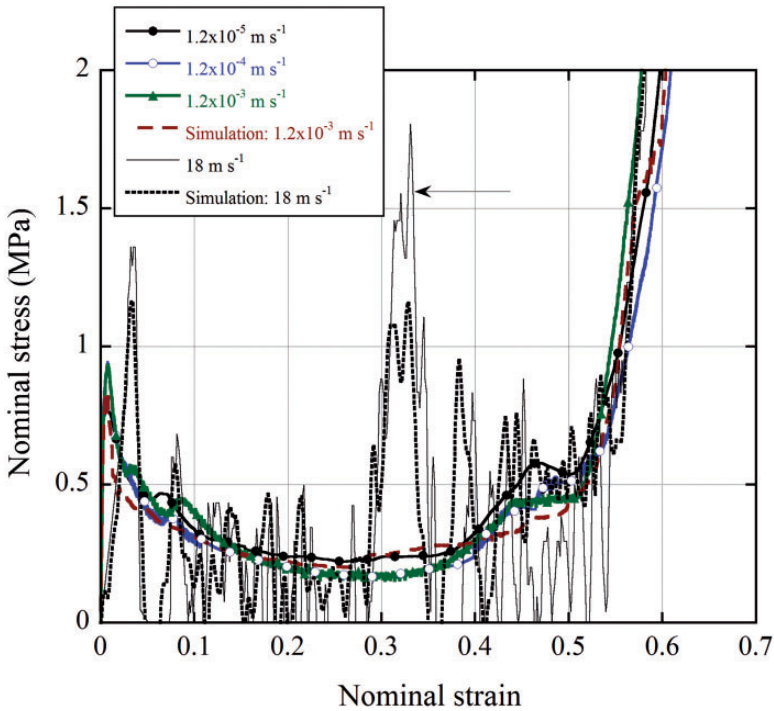


**Figure 11.** Experimental and numerical nominal stress–strain curves of single-layer sandwich at quasi-static and dynamic loading rates.

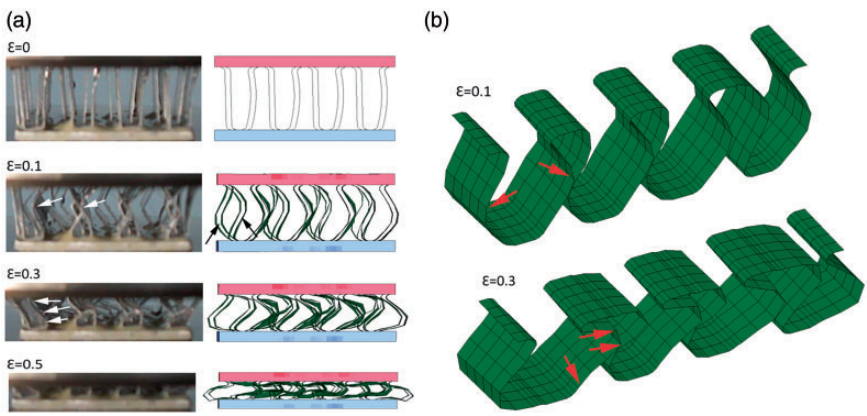


**Figure 12.** (a) Experimental and numerical deformation of single-layer sandwich and (b) numerical deformation of core fins at nominal strains of 0.1 and 0.3 at $1.2 \times 10^{-3}$ m s$^{-1}$.

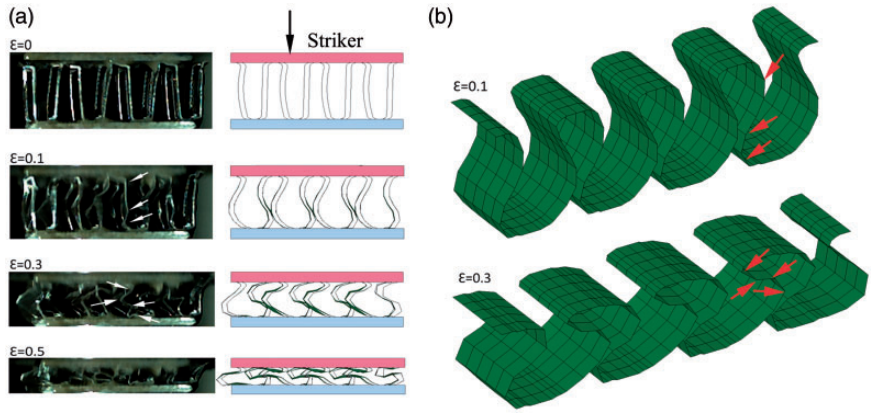


**Figure 13.** (a) Experimental and numerical deformation of single-layer sandwich and (b) numerical deformation of core fins at nominal strains of 0.1 and 0.3 at 18 m s$^{-1}$.

core fins at different nominal strains, respectively. The buckling mode of the fin wall at quasi-static loading rate is a mixed mode: the adjacent fin walls (normal to the sandwich front face) buckled numerically and experimentally in the opposite directions at nominal strain of 0.1 as shown with arrows in Figure 12(a) and (b). However, the buckling of the adjacent fin walls occurred in the same direction in dynamically tested single-layer sandwich as depicted in Figure 13(a) and (b). The fin buckling at quasi-static loading rate occurred at the center of the fin wall by forming three plastic hinges: two at the face sheets and one at the center of the wall. At dynamic loading rate, the fin walls, however, buckled initially near the impact side of the sandwich (striker bar side) and then at the lower section forming nearly an S-shape deformation with at least four plastic hinges as shown in Figure 13(b). The second instability occurred at nominal strain of 0.3 in dynamically tested samples, leading to the formation of a post-peak stress in the stress–strain curve. The increased stress levels at relatively high strains (>0.5) in Figure 11 are due to the compression of the folded fin walls, similar to the densification region in foam metal deformation [27]. Briefly, the fin buckling associates with relatively high buckling wavelength comparable with the size of the imperfection leading to reduced buckling stress and post-buckling stress at quasi-static loading rate, while the buckling mode of the dynamically tested samples occurred with relatively smaller wavelength leading to increased buckling stress.

The experimental and numerical nominal stress–strain curves of double-layer specimens tested at quasi-static ($2.2 \times 10^{-5}$, $2.2 \times 10^{-4}$, and $2.2 \times 10^{-3}$ m s$^{-1}$) and dynamic loading rates (18 m s$^{-1}$) are shown in Figure 14(a). The nominal stress–strain curves of double-layer specimen showed very similar trends with those of the single-layer specimen; however, the buckling stress (0.50–0.65 MPa) and post-buckling stress values were smaller than those of single-layer specimen. At quasi-static loading rates, the post-buckling region of the stress–strain curve remained

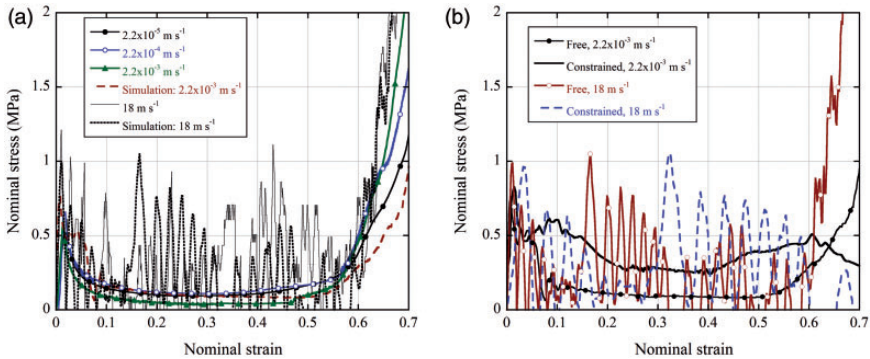


**Figure 14.** (a) Experimental and numerical nominal stress–strain curves of double-layer sandwich at quasi-static and dynamic loading rates and (b) the effect of constraining of interlayer sheet on nominal stress–strain curves.

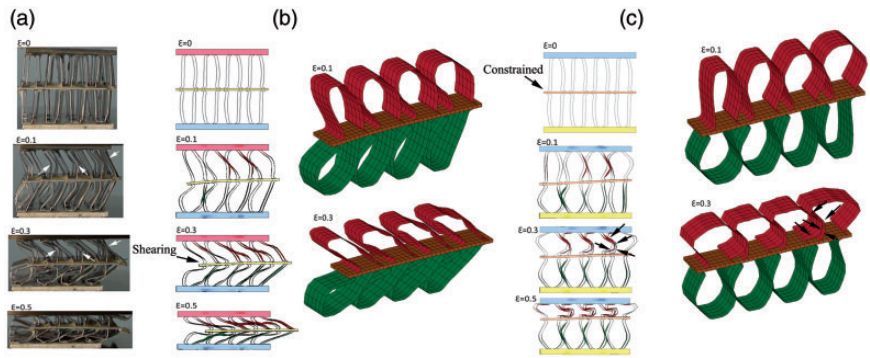


**Figure 15.** Deformation of double-layer sandwich and core fins; (a) experimental, (b) numerical and (c) numerical with constrained interlayer sheet at $2.2 \times 10^{-3}$ m s$^{-1}$.

smooth due to the shearing of the interlayer sheet as seen in Figure 15(a) and (b). Another effect of the interlayer shearing is on the deformation on fin walls; bending-type of deformation was seen to be dominant over buckling as depicted in numerical deformations of fins in Figure 15(b). However, the fin wall buckling became dominant over the interlayer sheet shearing at high loading rate as shown in Figure 16(a) and (b), leading to increased buckling and post-buckling stresses. At dynamic loading rate, the deformation localized on the top fin layer until about 0.3 strains; thereafter, the bottom fin layer started to collapse (Figure 16(a) and (b)). As with single-layer specimen, the stress values of double-layer specimen increased from 0.50 to 0.65 MPa at quasi-static loading rates to 1.2 MPa at dynamic loading rate. The peak stresses were observed in the plateau region of the dynamically tested samples due to complex buckling mechanisms of

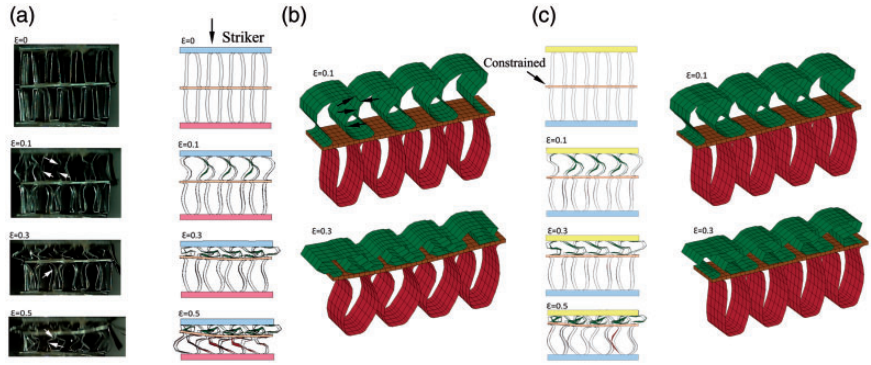


**Figure 16.** Deformation of double-layer sandwich and core fins; (a) experimental, (b) numerical and (c) numerical with constrained interlayer sheet at 18 m s$^{-1}$.

the fin layers. As with single-layer sandwich, double-layer sandwich showed velocity depending crushing stress simply arising from the change of the deformation mode of the fin walls from buckling and shearing to buckling at dynamic loading rate. Double-layer specimens showed lower buckling and post-buckling stresses than single-layer specimens at both quasi-static and dynamic loading rates, although the difference is more pronounced at quasi-static loading rates. A part of additional simulations were carried out by constraining the lateral movement of the interlayer sheet in double-layer specimens at quasi-static and dynamic loading rates. The effect of the constraining on crushing response of double-layer specimens is shown in Figure 14(b). At $2.2 \times 10^{-3}$ m s$^{-1}$, the initial peak stress was found to be similar for both cases; however, the post-buckling stresses were significantly increased by constraining the interlayer sheet. As shown in Figure 15(c), fin walls in the each layer buckles simultaneously up to nominal strain of 0.3, then fin layers collapsed progressively which led to increase in crushing stresses in post-buckling region. As result of this crushing behavior, the densification strain was also increased compared to the double-layer specimens experienced interlayer shearing. In dynamic loading rate, the initial peak stress was found to be insensitive to the constraining of interlayer sheet as shown in Figure 14(b). Constraining had also no effect on the value of the second peak stress in the post-buckling region; however, crushing of the bottom layer significantly delayed. Therefore, the second peak stress of the constrained double-layer specimen appeared around nominal strain of 0.28 as shown in Figure 14(b). This can be clearly seen from the numerical deformations of the double-layer specimens between nominal strains of 0.3 and 0.5 as depicted in Figure 16(b) and (c), respectively.

The relative error between experimental and numerical initial peak stresses at quasi-static and dynamic loading rates are given in Table 1. Numerical simulations of double-layer specimens at both loading rates predicted the initial stress with higher error in contrast to models of single-layer specimens. This was attributed to the shearing of the interlayer layer sheet.

**Table 1.** Relative error between experimental and numerical results of single- and double-layer corrugated core sandwiches at quasi-static and dynamic loading rates.

| | | Relative error (%) |
|---|---|---|
| Specimen | Loading rate (m $s^{-1}$) | Initial peak stress, $\sigma_i$ |
| Single-layer | $1.2 \times 10^{-3}$ | 9.67 |
| | 18 | 14.6 |
| Double-layer | $2.2 \times 10^{-3}$ | 28 |
| | 18 | 17.5 |

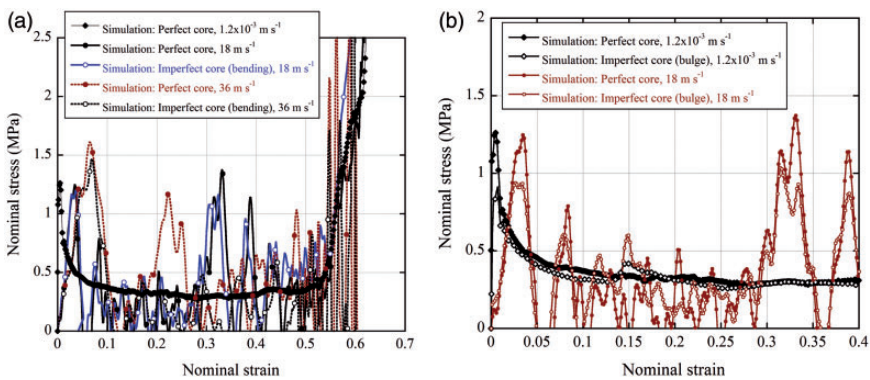


**Figure 17.** The effect of loading rate on nominal stress–strain curves of single-layer sandwiches; (a) perfect and bending type imperfect models and (b) perfect- and bulge-type imperfect models.

## *Effects of fin wall bending and bulging type of imperfections on crushing responses*

Figure 17(a) shows dynamic (18 and 36 m $s^{-1}$) nominal stress–strain curves of perfect and imperfect models together with that of the quasi-static perfect model for comparison. It was noted that the perfect and imperfect models gave nearly the similar buckling and post-buckling stresses at the loading rate of 18 m $s^{-1}$. The observed imperfection insensitive dynamic crushing behavior was also found previously in a corrugated core [11]. The perfect quasi-static model was also noted to have the similar buckling stress with the perfect model at 18 m $s^{-1}$. When the loading rate was increased numerically to 36 m $s^{-1}$, three effects were seen: the buckling stress increased over those of the loading rate of 18 m $s^{-1}$ and quasi-static perfect models; the perfect model showed slightly higher buckling stress

than imperfect model and a stress maximum appears at the strain of 0.2. At quasi-static loading rates, the imperfection sensitivity raised since the buckling wavelength was comparable with the size of the imperfection (9 mm), while at high loading rate, the buckling wavelength (~4.5 mm) got smaller than the imperfection size; hence, the structure became imperfection insensitive. The detected increase in the buckling stress at $36\,\mathrm{m\,s^{-1}}$ is due to the micro-inertial effect. When the imperfection size decreased from 9 mm to 1.5 mm (bulge-type imperfection), the structure became imperfection sensitive at both quasi-static and dynamic loading rates as depicted in Figure 17(b). In this case, the buckling wavelength for both quasi-static and high loading rate became larger than that of the imperfection size.

### *Comparison of crushing responses of zig-zag, straight and triangular corrugated core sandwiches*

The numerical quasi-static nominal stress–strain curves of the perfect zig-zag, straight trapezoidal and triangular corrugated core single-layer sandwiches and the corresponding deformation pictures at different nominal strains are shown in Figure 18(a) and (b), respectively. The buckling stresses of the zig-zag (1.25) and straight (1.30 MPa) corrugated core structures are very much similar, showing an insignificant effect of the zig-zag form on the buckling stress. Among the three corrugations, the triangular form exhibited the lowest buckling stress (1.04 MPa). As seen in Figure 18(b), the deformation modes of the corrugated single-layer sandwich samples are very much similar: the fin wall buckling, while the fin wall buckling in the zig-zag corrugated core sample is a mixed mode (Figure 18(b)). The buckling stresses of zig-zag (1.25 MPa) and straight trapezoidal (1.29 MPa) core single-layer sandwiches almost remained same when the loading rate was increased to $18\,\mathrm{m\,s^{-1}}$ (Figure 19(a)). However, the buckling stress of the triangular corrugated core single-layer sandwich increased to 1.40 MPa. The buckling mode of the zig-zag corrugated fin walls switched from mixed mode at quasi-static loading rate to single mode at dynamic loading rate as seen in Figure 19(b). In the following, the loading rate was doubled to $36\,\mathrm{m\,s^{-1}}$ numerically to determine anydeformation chances and inertial effects in the structures. When the loading rate was increased to $36\,\mathrm{m\,s^{-1}}$, the buckling stresses of the triangular and zig-zag and straight trapezoidal corrugated cores increased sequentially to 1.67, 1.61 and 1.57 MPa (Figure 20(a)). The unit fins of the zig-zag and straight trapezoidal and triangular corrugated core deformed similarly at the loading rate of $36\,\mathrm{m\,s^{-1}}$, leading to the appearance of the peak stresses in the plateau region at 0.2 strains. The deformation at increasing loading rates proceeded with the higher order of the buckling mode and the stabbing and the buckling of the fin wall took place (Figure 20(b)). It is noted in Figure 20(b) that the buckling length decreased when the loading rate was increased to $36\,\mathrm{m\,s^{-1}}$. The differences in both the initial loading and plateau regions between three corrugations got smaller at $36\,\mathrm{m\,s^{-1}}$ (Figure 20(a)). This was directly resulted from similar deformation behavior of the core layers under dynamic loading; initial buckling and continual crushing of the fin walls (Figure 20(b)).

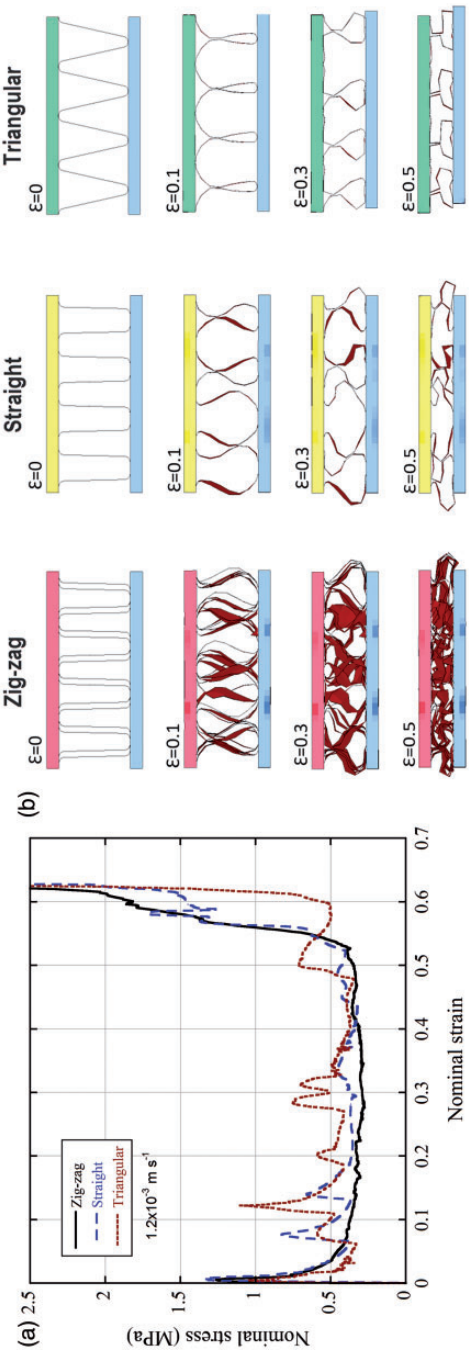


**Figure 18.** (a) Numerical nominal stress–strain curves and (b) deformations of single-layer zig-zag, straight and triangular corrugated core sandwiches at $1.2 \times 10^{-3}$ m s$^{-1}$.

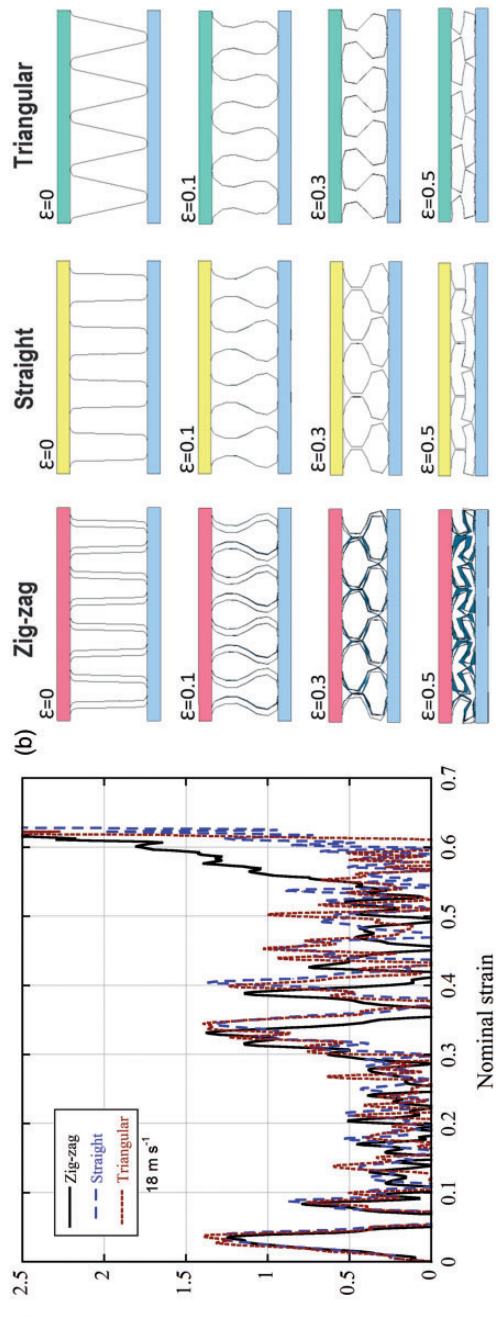


**Figure 19.** (a) Numerical nominal stress–strain curves and (b) deformations of single-layer zig-zag, straight and triangular corrugated core sandwiches at 18 m s$^{-1}$.

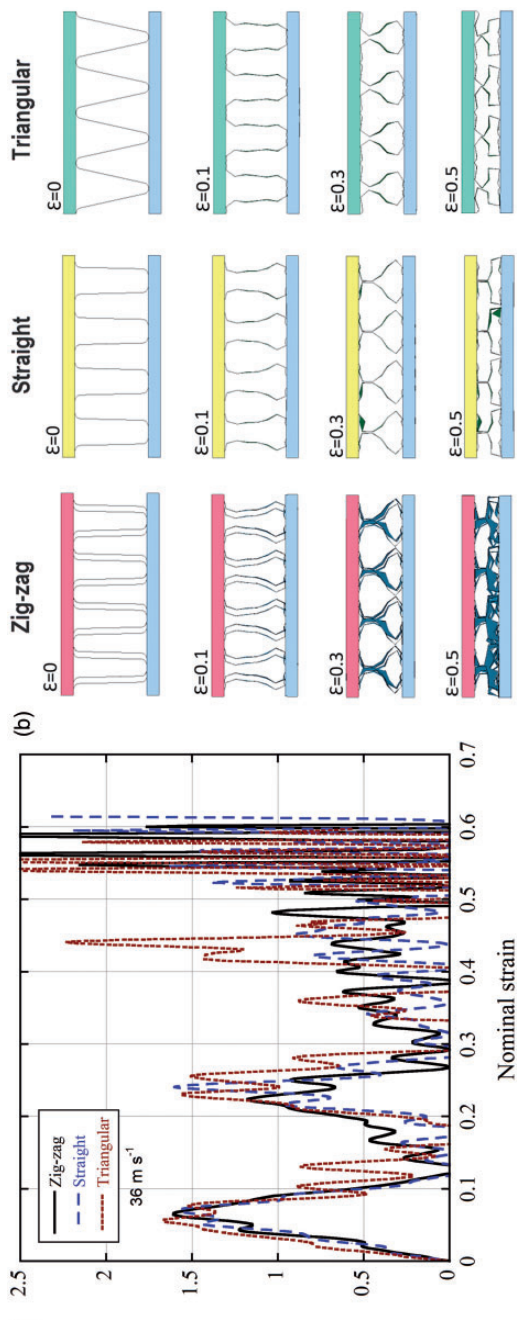


**Figure 20.** (a) Numerical nominal stress–strain curves and (b) deformations of single-layer zig-zag, straight and triangular corrugated core sandwiches at 36 m s$^{-1}$.

The triangular form of the corrugation showed higher and earlier micro-inertial effect than trapezoidal corrugated core.

The specific energy absorption of the tested single-layer corrugated core at quasi-static strain rate varies between 0.4 and 0.61 kJ kg$^{-1}$ at nominal strain of 0.57 corresponding to the displacement of abrupt increase in load values. These energy absorption values are comparable, by taking into account the densification strains, with the specific energy absorptions of mild steel V-, U-, X- and Y-type core structures varying between 0.94 and 4.04 kJ/kg, at the final strains between 0.66 and 0.85 [18]. The specific energy absorption of the tested corrugated structure increased to 1.31 kJ kg$^{-1}$ when the final strain increased to 0.66. The tested corrugated core also showed comparable specific energy absorption with the specific energy absorption of U-shaped glass, carbon and hybrid composite cores composite corrugated cores varying between 0.45 and 0.65 kJ kg$^{-1}$ [28].

The increased buckling stress of the studied corrugated sandwich structures with increasing loading rate may be considered separately for the imperfection sensitive and insensitive cases. In the former, the increasing loading rate from quasi-static to 18 m s$^{-1}$ changes the deformation from bending to stretching dominated mode for both single- and double-layer sandwiches, leading to increased buckling stresses. In a previous study, the peak stress of a unit metallic pyramidal truss core in the Hopkinson bar test was reported to be 60% higher than that in quasi-static test and the increased compressive stress at increasing strain rates was attributed to strain rate sensitive flow stress of stainless steel and inertial effects [3]. The structures exhibiting a relatively flat-topped quasi-static load displacement curve are classified as Type I, while the structures exhibiting a steeply declining quasi-static load-displacement curve following an initial peak load are classified as Type II structure [12]. Examples of Type I and Type II structures are the lateral and axial compression of beams and tubes, respectively. When the kinetic energy of impact was kept constant, the smaller final displacements of Type II structures were measured at increasing impact velocities [12,29]. Type II structures are more inertia and strain rate sensitive than Type I structures. The tendency of energy absorption of Type II structures was shown to be enhanced by the structure material strain rate sensitivity [29–31]. Tam and Calladine [29] analyzed the deformation of Type II structures based on a rigid-plastic analysis in two phases. The first phase involves the plastic compression of the structure, while the second phase involves the rotations of plastic hinges. It was reported that the inertia is the dominant in the first phase and the strain rate sensitivity is dominant in the second phase. Su et al. [31,32] proposed an elastic plastic model for the compression of Type II structures and concluded that inertia and strain rate sensitivity were dominant in the entire deformation processes. It was also reported in the same studies that an elastic analysis were necessary in order to determine the magnitude of the peak load. The corrugated structures tested in the present study also show inertia-sensitive Type II behavior. The propagation of the plastic wave at high strain rates delays the overall buckling of the member and the member needs to form kinks [33]. The phenomenon of kink formation at high strain rate is also seen in the experimentally

tested single- and double-layer sandwiches (shown in Figure 10(c) by white arrows). When the imperfection size is comparably smaller than the buckling wavelength, imperfection insensitive case, the inertial effects appear at higher loading rates, $36\,m\,s^{-1}$.

## Conclusions

The axial crushing response of layered 1050 H14 aluminum zig-zag trapezoidal single- and double-layer corrugated core sandwich structures was determined experimentally and numerically at quasi-static and dynamic loading rates. The effect of induced fin wall imperfection was simulated by the imperfect models of fin wall bending and fin wall bulging. The fin wall bending-type imperfection model well simulated the experimental quasi-static and dynamic nominal stress–strain curves of the tested sandwiches. The buckling stress of the corrugated sandwich structures increased when the loading rate was increased from quasi-static to $18\,m\,s^{-1}$. The increased buckling stresses were ascribed to micro-inertial effects, which altered the deformation mode of single-layer sandwiches from buckling of three plastic hinges at quasi-static loading rate to higher number of plastic hinge (kink) formations at high loading rate. Although shearing of interlayer sheet was seen to be the main deformation mechanism in double-layer sandwiches at quasi-static loading rates, inertial effects at dynamic strain rates changed the deformation mode into fin buckling. Dynamic strain rate induced a confining effect on the deformation of the corrugated layers. The buckling stress at quasi-static and high loading rates was shown numerically imperfection sensitive when the imperfection size was reduced below the buckling length, while at larger imperfection size the structure became imperfection sensitive at quasi-static loading rates. The simulations also showed that the inertial effects appeared at higher loading rates for the perfect structure or when the imperfection size was smaller than the buckling wavelength. The simulations based on the perfect model at $36\,m\,s^{-1}$ clearly indicated earlier micro-inertial effect in the triangular form of the corrugation was higher than the trapezoidal corrugated cores. The numerical buckling stresses of the zig-zag and straight corrugated core structures were shown to be similar at both quasi-static and high loading rates, implying an insignificant effect of the zig-zag form. Finally, the tested single-layer corrugated core at quasi-static strain rate showed comparable specific energy absorption with metal and composite corrugated cores.

### Acknowledgments

The authors would like to thank Cumhur Akar for providing corrugated aluminum core samples.

### Declaration of conflicting interests

The author(s) declared no potential conflicts of interest with respect to the research, authorship, and/or publication of this article.

## Funding

The author(s) received no financial support for the research, authorship, and/or publication of this article.

## References

1. Wadley HNG. Multifunctional periodic cellular metals. *Philos Trans R Soc A-Math Phys Eng Sci* 2006; 364: 31–68.
2. Radford DD, Fleck NA and Deshpande VS. The response of clamped sandwich beams subjected to shock loading. *Int J Impact Eng* 2006; 32: 968–987.
3. Lee S, Barthelat F, Hutchinson JW, et al. Dynamic failure of metallic pyramidal truss core materials – experiments and modeling. *Int J Plasticity* 2006; 22: 2118–2145.
4. Tilbrook MT, Radford DD, Deshpande VS, et al. Dynamic crushing of sandwich panels with prismatic lattice cores. *Int J Solids Struct* 2007; 44: 6101–6123.
5. Yungwirth CJ, Wadley HNG, O'Connor JH, et al. Impact response of sandwich plates with a pyramidal lattice core. *Int J Impact Eng* 2008; 35: 920–936.
6. Rubino V, Deshpande V and Fleck N. The dynamic response of end-clamped sandwich beams with a Y-frame or corrugated core. *Int J Impact Eng* 2008; 35: 829–844.
7. Rubino V, Deshpande VS and Fleck NA. The dynamic response of clamped rectangular Y-frame and corrugated core sandwich plates. *Eur J Mech A-Solid* 2009; 28: 14–24.
8. McShane GJ, Deshpande VS and Fleck NA. Underwater blast response of free-standing sandwich plates with metallic lattice cores. *Int J Impact Eng* 2010; 37: 1138–1149.
9. Liang Y, Louca L and Hobbs R. Corrugated panels under dynamic loads. *Int J Impact Eng* 2007; 34: 1185–1201.
10. Cote F, Deshpande V, Fleck N, et al. The compressive and shear responses of corrugated and diamond lattice materials. *Int J Solids Struct* 2006; 43: 6220–6242.
11. McShane GJ, Pingle SM, Deshpande VS, et al. Dynamic buckling of an inclined strut. *Int J Solids Struct* 2012; 49: 2830–2838.
12. Calladine CR and English RW. Strain-rate and inertia effects in the collapse of two types of energy-absorbing structure. *Int J Mech Sci* 1984; 26: 689–701.
13. Zhao H, Elnasri I and Abdennadher S. An experimental study on the behaviour under impact loading of metallic cellular materials. *Int J Mech Sci* 2005; 47: 757–774.
14. Langseth M and Hopperstad OS. Static and dynamic axial crushing of square thin-walled aluminium extrusions. *Int J Impact Eng* 1996; 18: 949–968.
15. Paul A and Ramamurty U. Strain rate sensitivity of a closed-cell aluminum foam. *Mater Sci Eng A Struct* 2000; 281: 1–7.
16. Reid SR and Peng C. Dynamic uniaxial crushing of wood. *Int J Impact Eng* 1997; 19: 531–570.
17. Tagarielli VL, Deshpande VS and Fleck NA. The high strain rate response of PVC foams and end-grain balsa wood. *Compos Part B-Eng* 2008; 39: 83–91.
18. Zhang YC, Zhang SL and Wang ZL. Crush behavior of corrugated cores sandwich panels. In: Zhou M (ed.) *High performance structures and materials engineering, pts 1 and 2*. Stafa-Zurich: Trans Tech Publications Ltd, 2011, pp.1584–1589.
19. Kilicaslan C, Odaci IK, Tasdemirci A, et al. Experimental testing and full and homogenized numerical models of the low velocity and dynamic deformation of the trapezoidal aluminium corrugated core sandwich. *Strain* 2014; 50: 236–249.

20. Kilicaslan C, Guden M, Odaci IK, et al. The impact responses and the finite element modeling of layered trapezoidal corrugated aluminum core and aluminum sheet interlayer sandwich structures. *Mater Des* 2013; 46: 121–133.
21. E 8M-04: Standard specification for standard test methods for tension testing of metallic materials *ASTM Standard*. ASTM International, 2004.
22. *LS-DYNA Keyword User's Manual*. Livermore Software Technology Corporation (LSTC), 2007, p.1384.
23. Gumruk R and Karadeniz S. A numerical study of the influence of bump type triggers on the axial crushing of top hat thin-walled sections. *Thin Wall Struct* 2008; 46: 1094–1106.
24. Johnson W and Mamalis AG. A survey of some physical defects arising in metal working processes. In: *Proceedings of the 17th International MTDR Conference*. Birmingham, U.K., September 1976, Macmillan, London, 1977, pp.607–21.
25. Smerd R, Winkler S, Salisbury C, et al. High strain rate tensile testing of automotive aluminum alloy sheet. *Int J Impact Eng* 2005; 32: 541–560.
26. Santosa SP, Wierzbicki T, Hanssen AG, et al. Experimental and numerical studies of foam-filled sections. *Int J Impact Eng* 2000; 24: 509–534.
27. Gibson LJ. The mechanics of foams: basic results. In: Gibson LJ and Michael F (eds) *Cellular solids: structure & properties*, Oxford/New York: Pergamon Press, 1988.
28. Zhang J, Supernak P, Mueller-Alander S, et al. Improving the bending strength and energy absorption of corrugated sandwich composite structure. *Mater Des* 2013; 52: 767–773.
29. Tam LL and Calladine CR. Inertia and strain-rate effects in a simple plate-structure under impact loading. *Int J Impact Eng* 1991; 11: 349–377.
30. Zhang TG and Yu TX. A note on a velocity sensitive energy-absorbing structure. *Int J Impact Eng* 1989; 8: 43–51.
31. Su XY, Yu TX and Reid SR. Inertia-sensitive impact energy-absorbing structures part II: effect of strain-rate. *Int J Impact Eng* 1995; 16: 673–689.
32. Su XY, Yu TX and Reid SR. Inertia-sensitive impact energy-absorbing structures part I: effects of inertia and elasticity. *Int J Impact Eng* 1995; 16: 651–672.
33. Vaughn DG, Canning JM and Hutchinson JW. Coupled plastic wave propagation and column buckling. *J Appl Mech-T Asme* 2005; 72: 139–146.